



Article

Gas Sensing Performance of Zinc Oxide Nanoparticles Fabricated via *Ochradenus baccatus* Leaf

Mohd Wajid Ali Khan^{1,2}, Nagih M. Shaalan^{3,4} , Faheem Ahmed^{5,*}, Subuhi Sherwani^{2,6,*}, Abdullah Aljaafari³ , Abdulmohsen K. D. Alsukaibi^{1,2}, Khalaf M. Alenezi^{1,2} and Khalid Al-Motair²

¹ Department of Chemistry, College of Sciences, University of Ha'il, Ha'il 55473, Saudi Arabia; mw.khan@uoh.edu.sa (M.W.A.K.); a.alsukaibi@uoh.edu.sa (A.K.D.A.); k.alenezi@uoh.edu.sa (K.M.A.)

² Medical and Diagnostic Research Center, University of Ha'il, Ha'il 55473, Saudi Arabia; k.almutier@uoh.edu.sa

³ Department of Physics, College of Sciences, King Faisal University, Al-Ahsa 31982, Saudi Arabia; nmohammed@kfu.edu.sa (N.M.S.); aaljaafari@kfu.edu.sa (A.A.)

⁴ Physics Department, Faculty of Science, Assiut University, Assiut 71516, Egypt

⁵ Department of Applied Sciences & Humanities, Faculty of Engineering & Technology, Jamia Millia Islamia, New Delhi 110025, India

⁶ Department of Biology, College of Sciences, University of Ha'il, Ha'il 55473, Saudi Arabia

* Correspondence: fahmed@jmi.ac.in (F.A.); s.sherwani@uoh.edu.sa (S.S.)

Abstract: ZnO nanoparticles (NPs) were prepared by green synthesis using plant leaf extraction of *Ochradenus baccatus* and characterized by XRD, FESEM, HRTEM, and Raman spectroscopy techniques. Since elevated CO levels have been associated with inflammatory conditions, cardiovascular diseases, and respiratory disorders and the methane gas primarily produced by gut microbiota and linked to gastrointestinal disorders and other abnormal methane levels in breath samples, the nanoparticles were applied for gas sensor fabrication. Thus, the gas sensors fabricated using ZnO nanoparticles were investigated for CH₄, H₂, CO, and NO₂ gases. The gas sensing was performed for the fabricated sensors at various operating temperatures and gas concentrations. Interestingly, leaf-extracted green synthesized ZnO NPs were more sensitive to CH₄, CO, and NO₂ gases than to H₂. The results of sensing studies revealed that the nanoparticles exhibit a selectivity toward gas depending on the gas type. The sensor response was also studied against the humidity. These findings bridge between the laboratory and industry sectors for future gas sensors development, which can be used for exhaled breath analysis and serve as potential diagnostic tools for highly sensitive contagious diseases.

Keywords: exhaled breath analysis; gas sensor; nanoparticles; CO; CH₄; NO₂; plant extraction; diagnostic; contagious diseases



Citation: Khan, M.W.A.; Shaalan, N.M.; Ahmed, F.; Sherwani, S.; Aljaafari, A.; Alsukaibi, A.K.D.; Alenezi, K.M.; Al-Motair, K. Gas Sensing Performance of Zinc Oxide Nanoparticles Fabricated via *Ochradenus baccatus* Leaf. *Chemosensors* **2024**, *12*, 28. <https://doi.org/10.3390/chemosensors12020028>

Academic Editors: Fanli Meng, Zhenyu Yuan and Dan Meng

Received: 5 January 2024

Revised: 9 February 2024

Accepted: 13 February 2024

Published: 16 February 2024



Copyright: © 2024 by the authors. Licensee MDPI, Basel, Switzerland. This article is an open access article distributed under the terms and conditions of the Creative Commons Attribution (CC BY) license (<https://creativecommons.org/licenses/by/4.0/>).

1. Introduction

A substantial surge in environmental contamination, driven by rapid industrialization, population expansion, the combustion of vehicular fuels, the widespread use of pesticides and insecticides in agriculture, and the release of toxic chemicals and gases, poses a significant and alarming threat to the ecosystems within our biosphere [1]. Over recent decades, there has been considerable interest in transition metal oxide materials, owing to their distinctive physical and chemical characteristics, which have created promising opportunities for their utilization in environmental surveillance and catalysis [1–3]. Within the realm of transition metal oxides, zinc oxide (ZnO) stands out as a highly promising material for environmental applications, primarily due to its exceptional thermal and chemical stability [4]. ZnO has garnered considerable attention in the context of chemical sensor development. This is attributed to its distinctive physical and chemical attributes, wide spectrum of radiation absorption, and exceptional photostability, rendering it a versatile material [5]. In the field of materials science, ZnO is categorized as a semiconductor within the II–VI group, exhibiting covalent characteristics that straddle the boundary

between ionic and covalent semiconductors. Its wide energy bandgap of 3.37 eV renders ZnO an attractive candidate for potential applications in electronics, optoelectronics, and laser technology [6,7].

Since the pioneering use of ZnO nanostructures in gas sensor applications, a substantial body of literature has emerged, detailing investigations into the synthesis and properties of ZnO nanostructures. For instance, multiple techniques for the growth of ZnO nanostructures have been reported. Various methods are employed in diverse ZnO nanostructure growth using an electrochemical approach [8], template-based growth, and sol-gel processing [9,10]. Another effective solution-based method is the hydrothermal process, allowing for the growth of these nanostructures at relatively low temperatures. Furthermore, ZnO nanostructures have been synthesized through alternative means such as electrospinning [11], a two-step mechanochemical-thermal process [12], chemical vapor deposition (CVD) [13], sonochemical synthesis [14], microwave-assisted combustion [15], anodization [16], and precipitation [17].

Despite the commonly used synthesis procedure mentioned above, there are some concerns related to the cost, time, and energy consumption and the generation of multiple hazardous chemicals by-products. Therefore, a green route for the synthesis of ZnO, which could be non-toxic, environmentally friendly, and cost-effective, is highly desired. Furthermore, the ZnO nanoparticles prepared using the green route are water-soluble, as there is no requirement for organic solvent, and the synthesis can be carried out at ambient temperature and pressure; thus, complex reaction systems are not needed. Among green synthesis routes, the plant extraction method using various green sources including leaf extracts, fruits, and other plant species is highly promising [18–20]. While all these fabrication methods contribute to the development of gas sensors based on nanostructures, they still pose significant challenges, particularly in terms of cost and reproducibility. The pressing need for straightforward, cost-effective fabrication techniques is driven by the quest for novel chemical sensors with enhanced performance attributes, particularly concerning selectivity, sensitivity at very low concentrations, stability, and operational temperature. Consequently, the scientific community and researchers have increasingly focused on refining these aforementioned factors. Extensive research was conducted to identify the ideal morphology and crystallographic configuration of zinc-oxide-based chemical sensors, employing various synthesis methods [21–24]. Research findings have demonstrated that ZnO exhibits remarkable sensitivity to various gases [25–32].

Gas sensors have emerged as promising tools in disease diagnosis, leveraging their ability to detect specific volatile organic compounds (VOCs) associated with various medical conditions. The potential applications of gas sensors were applied for diagnosing diseases through the detection of carbon monoxide (CO) and methane (CH₄), highlighting their role as non-invasive biomarkers [33]. Carbon monoxide is a gaseous molecule produced during heme degradation, and its levels can vary in different disease states. Elevated CO levels have been associated with inflammatory conditions, cardiovascular diseases, and respiratory disorders [33]. Gas sensors designed to detect CO concentrations in exhaled breath or bodily fluids hold promise for non-invasive disease diagnosis. Carbon monoxide has been described as one of the highest common sources of death, making up 31% of toxic poisoning cases. Carbon monoxide causes accidental death associated with breathing at high levels, as it is both odorless and tasteless [34]. Carbon monoxide is absorbed unchanged by the lung, where 90% is bound to hemoglobin (Hb), 10% to myoglobin, and 10% to cytochromes. About 1% of CO is dissolved in plasma, and less than 1% of CO is oxidized to carbon dioxide [34]. Methane, primarily produced by gut microbiota, has been linked to gastrointestinal disorders. Abnormal methane levels in breath samples have been identified in conditions such as irritable bowel syndrome (IBS) and other gastrointestinal diseases [35–38]. Gas sensors sensitive to methane can potentially aid in the early diagnosis and monitoring of such disorders.

In this study, ZnO nanoparticles were prepared by a green route, using the plant extract of *Ochradenus baccatus* as a biotemplate, and utilized as gas sensors to test various

reducing gases, namely CH₄, H₂, CO, and oxidizing NO₂ gas. To the best of our knowledge, the synthesis of ZnO nanoparticles using leaf extraction of *Ochradenus baccatus* and their utilization in the gas sensing of oxidizing and reducing gases simultaneously has not been reported. The gas sensor measurement was performed by resistance measurements of systematically conducted variants across a range of temperatures, specifically at 200, 250, 300, and 350 °C. The sensing results revealed that the fabricated nanoparticles exhibit heightened sensitivity towards CH₄ and CO gases. Conversely, nanoparticles display superior sensitivity at 200, 250, and 300 °C, demonstrating exceptional performance, particularly in the detection of reducing gases of CO, CH₄, and oxidizing NO₂ gas. The nanoparticle gas sensor exhibited high repeatability and stability. The humidity effect on the sensor response was also demonstrated.

2. Materials and Methods

2.1. Preparation of ZnO Nanoparticles

Analytical-grade reagents were used throughout the study. Zinc nitrate (99.999%) was procured from Sigma-Aldrich (St. Louis, MO, USA). The synthesis procedure was executed using a household microwave oven (Samsung, 750 W, Suwon-si, Republic of Korea). For the extraction of *Ochradenus baccatus* plant, the leaves of *Ochradenus baccatus* were collected from mature plants available. The extraction was carried out using a speed extractor (Buchi, E-914, Essen, Germany), and a metal frit and cellulose filter were inserted at the bottom of the stainless-steel cell. Then, 5–10 g of *Ochradenus baccatus* leaves was cleaned thoroughly with ultrapure water and ethanol several times, and then the leaves were cut into small pieces and dried in an oven at 60 °C overnight and then crushed into a fine powder. The obtained fine powder was then transferred to the cell extractor and run for two cycles for 45 min each, and the temperature was kept fixed at 60 °C. For the utilization of leave extract, 50 mL of water was filtered, and the concentrated water extract was obtained and used. In a typical experimental setup, an aqueous solution of zinc nitrate (0.05 M) in 100 mL of distilled water was prepared, and then 10 mL of *Ochradenus baccatus* leaf extract was introduced, forming a mixed solution within the flask. Subsequently, the flask was positioned in a common household microwave oven and run for 15–20 min. The solution was cooled to bring the temperature to 25 °C. The precipitate formed was separated via centrifugation. Precipitate was washed repeatedly with deionized water and absolute ethanol and then oven dried for 24 h at 80 °C. Ultimately, the product underwent calcination at 800 °C for 2 h.

2.2. Characterizations

Phase purity analysis of the resulting product was conducted using X-ray diffraction, employing a Rigaku (Miniflex-2) X-ray diffractometer with Cu K α radiation ($\lambda = 1.5406 \text{ \AA}$). This instrument functioned at a voltage of 40 kV and a current of 15 mA. For the assessment of particle size and surface morphology, high-resolution transmission electron microscopy (HRTEM; JEOL/JEM-2100F version) at 200 kV was utilized. For the examination of surface morphology, we utilized a field emission scanning electron microscope (FESEM; JEOL-7600). Raman spectroscopy was performed using a LabRAM HR800 confocal micro-Raman spectrometer, outfitted with a multichannel charge-coupled detector. A He-Cd laser, with a wavelength of 442 nm and an output power of 20 mW, was utilized as the excitation source. The Raman spectrometer incorporated 1800 lines per millimeter (1/mm) gratings. Raman spectra were captured under backscattering geometry, ensuring a spectral resolution of 0.8 cm^{-1} at ambient room temperature.

2.3. Gas Sensor Preparation and Characterizations

Considering that the sensing materials were in powder form, the process of sensor fabrication proceeded as follows: Firstly, two gold electrodes were deposited onto a glass substrate using DC sputtering and using a mechanical mask with a 400 μm gap. Secondly, a screen-printing method was employed to coat the substrate with the sensing materials,

resulting in a thickness of approximately 50 μm . The screen/mask was homemade from Stainless Steel 304 grade 0.05 mm in thickness and 100 mm² in area, which was preprocessed with fiber laser to make a hole of 7 \times 7 mm². For sensor fabrication, the slurry was made by taking 90% of the sensing material and 10% of the polyvinylidene difluoride (PVDF) binder in an agate mortar and mixing by 1-methyl-2-pyrrolidone (NMP) solvent drops into a fabricated paste. Then, a layer was coated on the gold electrode using the stainless-steel mask. The sensor was then dried overnight at 80 $^{\circ}\text{C}$ and then calcinated at 400 $^{\circ}\text{C}$ for two hours, since the sensor will work at high temperatures.

The detected gases were balanced in the cylinders as follows: CH₄ (1%) was balanced with synthetic air, CO (1%) was balanced with nitrogen to avoid transformation to carbon dioxide, NO₂ (50 ppm) was balanced with synthetic air, and H₂ (1%) was balanced with synthetic air. For gas sensor testing, a controlled flow of dry synthetic air blended with gases such as H₂, CO, CH₄, and NO₂ was introduced into the measurement chamber at a flow rate of 200 mL/min with the HORIBA MFCs-N100 series. Electrical measurements were performed using a computerized data acquisition instrument (multichannel LXI-Agilent 34972A), as shown in Figure 1a,b. The operational temperature of the sensor ranged from 200 $^{\circ}\text{C}$ to 350 $^{\circ}\text{C}$ and was controlled by the temperature-controlled chamber of Linkam model HFS 600 E—PB 4 probe thermal stage. The sensor response was characterized as the ratio of electrical resistance change, represented as $\Delta R/R_g$ (for reducing gases) and $\Delta R/R_a$ (for oxidizing gases), where R_a signified the resistance in synthetic air, and R_g represented the resistance in the presence of the target gas.

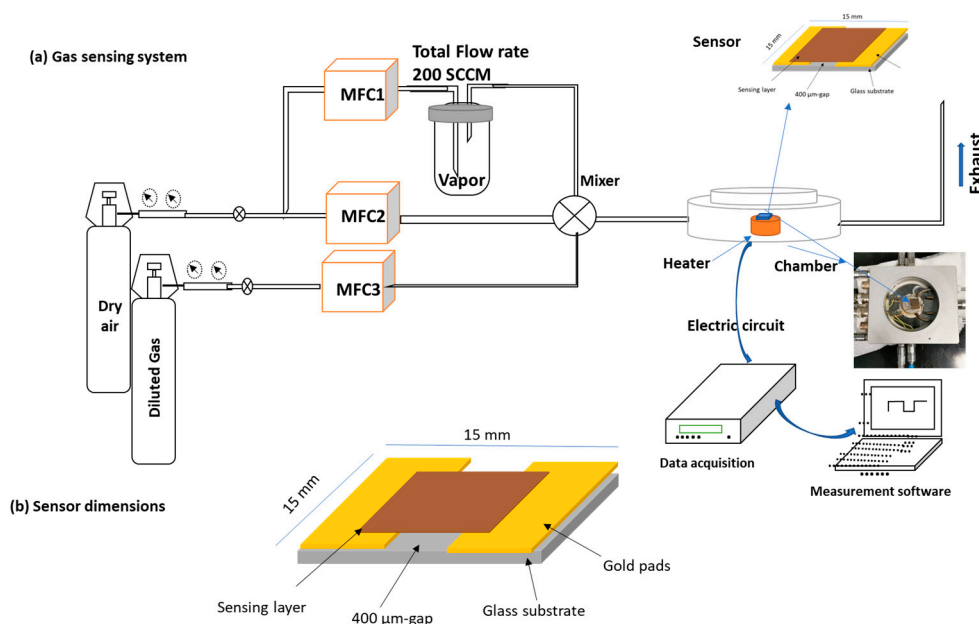


Figure 1. Scheme of (a) the gas sensing measurement system and (b) dimensions of the sensor.

3. Results and Discussion

3.1. Structural and Morphology of ZnO NPs

Figure 2 shows the X-ray diffraction (XRD) patterns of ZnO nanoparticles. All diffraction peaks were indexed using POWDER-X software (ver. 2017) as the ZnO wurtzite structure, closely aligning with the standard data (JCPDS, 36-1451) for ZnO nanoparticles. Notably, these patterns distinctly reveal that the material exhibited a single-phase pattern, displaying the hexagonal wurtzite structure. Following refinement, the prepared ZnO was found to have lattice parameters of $a = 3.253 \text{ \AA}$ and $c = 5.246 \text{ \AA}$, respectively. These values closely match those within the standard database (JCPDS, 36-1451). Furthermore, the enhanced peak intensities of all diffraction peaks in the product's XRD patterns signify the high crystallinity exhibited by the obtained ZnO nanoparticles.

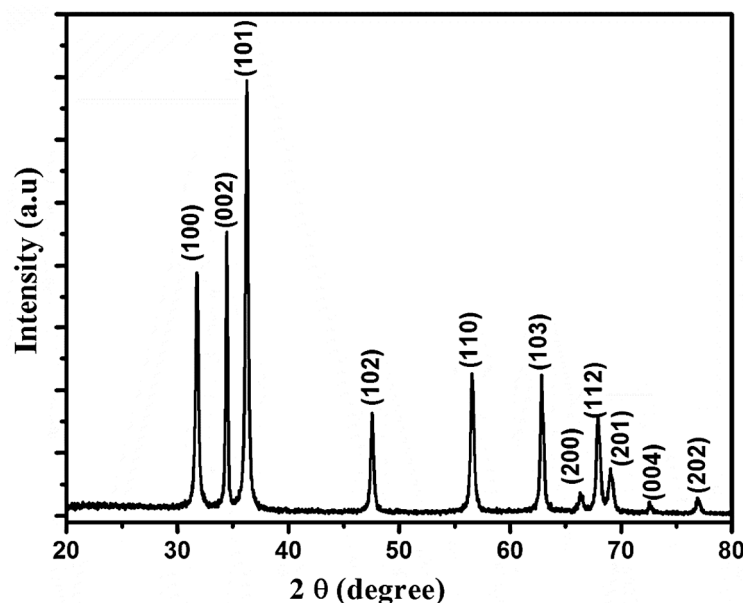


Figure 2. X-ray diffraction (XRD) patterns of ZnO nanoparticles.

The crystal size of the product was determined by analyzing the broadening of X-ray diffraction lines, employing Scherer's equation [39]:

$$D = 0.89 \lambda / (\beta \cos \theta) \quad (1)$$

where λ is the wavelength (Cu K α), β is the full width at the half maximum, and θ is the diffraction angle. The average crystallite size of ZnO nanoparticles was found to be ~56 nm.

Figure 3a,b exhibit FESEM images of ZnO nanoparticles. FESEM images with low and high magnifications showed the particle size distributed between 50 and 110 nm. According to the TEM images, a homogeneous distribution of particle size of approximately ~78 nm was observed (Figure 3c), confirming that the particles observed in the SEM image gathered 2–4 grains or crystallites. The agglomeration phenomenon is attributed to the compacting effect induced by the narrow inter-particle spacing, facilitated by the equivalent distribution of oxidized metal anions within the network's three-dimensional structure. Notably, TEM micrographs, as shown in Figure 3d, reveal a morphology of mixed spherical and elongated rod-shaped particles. The inset of Figure 3d shows the HRTEM image of the ZnO nanoparticles. This HRTEM image reveals distinct lattice fringes, signifying the presence of the crystalline wurtzite structure of ZnO, as evidenced by d-spacing values consistent with established standard data for ZnO.

ZnO, possessing a wurtzite structure and classified as the simplest uniaxial crystals, falls within the C_{6v}^4 ($P6_3 mc$) space group. Within the context of an ideal ZnO crystal, the optical phonons located at the Γ point within the Brillouin zone participate in first-order Raman scattering. Group theory anticipates the following optic modes: $\Gamma_{opt} = A_1 + 2B_1 + E_1 + 2E_2$. Under this paradigm, both A_1 and E_1 modes demonstrate polarity and subdivision into transverse optical (A_1^{TO} and E_1^{TO}) as well as longitudinal optical (A_1^{LO} and E_1^{LO}) components. The E_2 mode includes two phonon modes with varying frequencies, specifically E_2^{low} and E_2^{high} , linked with the vibrational movement of the respective Zn sublattice and oxygen atoms. Following the Raman selection rule [40,41], all aforementioned modes are classified as Raman-active modes of the first order. Furthermore, the B_1 branch remains inactive, while the frequencies for the B_1^{low} and B_1^{high} modes have been computed as 260 and 540 cm^{-1} , respectively [42,43]. Figure 4 displays the Raman spectrum of ZnO nanoparticles. Under the Raman selection rule, the B_1 modes are typically inactive in Raman spectra and referred to as silent modes [43]. The fundamental phonon modes of hexagonal ZnO for ZnO nanoparticles have been identified and correspond to

E_{2L} , E_{2H} , and $A_1(LO)/E_1(LO)$. Furthermore, multiple phonon scattering modes are evident and can be attributed to $3E_{2H}-E_{2L}$, $2(E_{2H}-E_{2L})$, and $A_1(TO) + E_1(TO) + E_{2L}$, respectively.

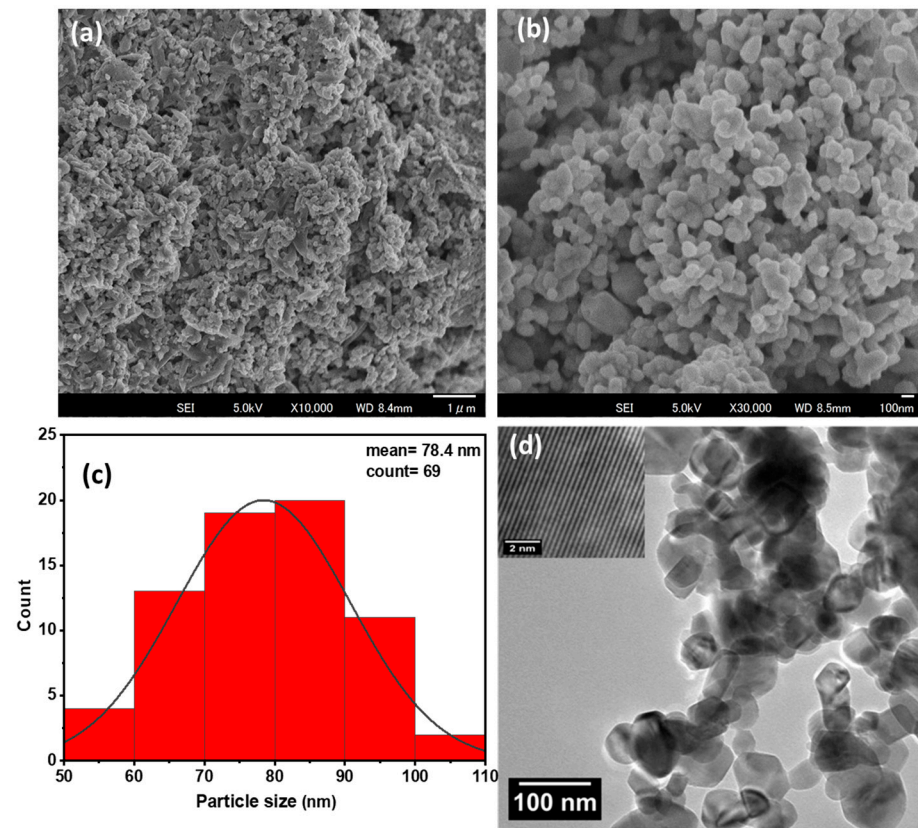


Figure 3. Surface morphology of (a) low- and (b) high-magnification FESEM images of ZnO nanoparticles, (c) histogram of particle distribution from FESEM images, and (d) a TEM micrograph with the inset showcasing the corresponding HRTEM image.

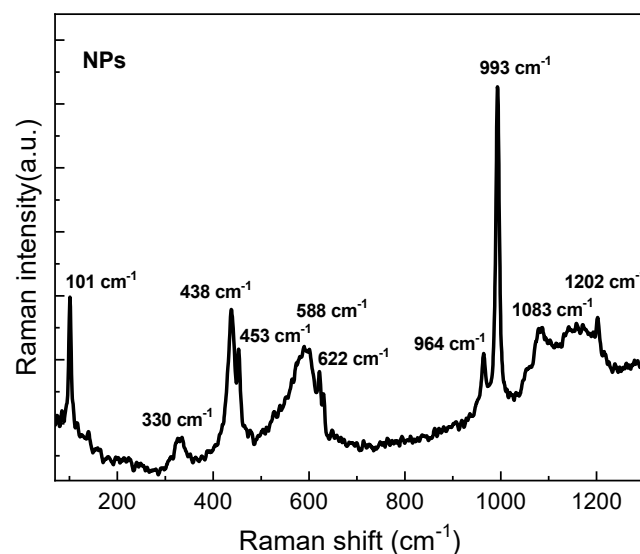


Figure 4. Raman spectrum of ZnO nanoparticles at room temperature.

3.2. Gas Sensing Properties of ZnO NPs

The sensing characteristics of ZnO nanoparticle (NP) sensors were systematically examined across various operating temperatures, focusing on their response to reducing gases such as CH_4 , CO , H_2 , and oxidizing NO_2 gas. Figure 5 depicts the variation in

resistance exhibited by the NP sensor when exposed to 1.0% CH₄, 0.1% CO, and 5 ppm NO₂, respectively. It is noteworthy that upon exposure to reducing gases, the sensor resistance decreases, while with exposure to 5 ppm NO₂, the sensor resistance exhibits an increase indicating that the ZnO-assembled nanostructures exhibited n-type semiconductor behavior. It is important to mention that no response from the sensors was observed at temperatures below 200 °C, and a very low signal toward H₂ was observed (not shown here). At 200 °C, the significant shift in the sensor's reaction can be ascribed to the heightened surface activity associated with higher temperatures, as the sensing phenomenon primarily occurs at the surface. In simpler terms, the chemical reactions involving adsorbed oxygen molecules on the oxide's surface transform, as previously reported by Ruhlan et al. [44], as illustrated in the chemical equations.

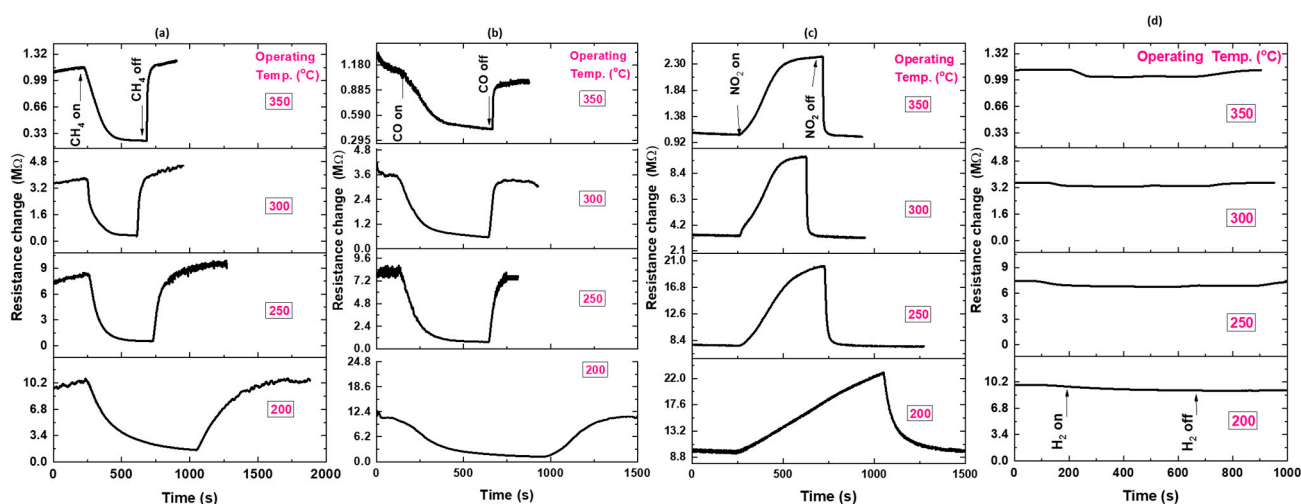
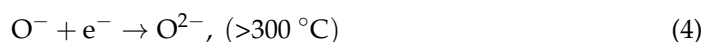
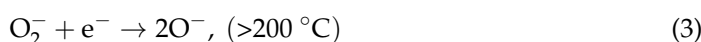
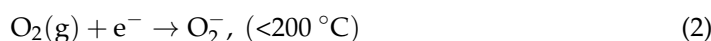
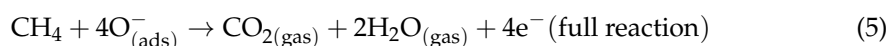


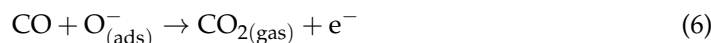
Figure 5. Sensor signals towards (a) CH₄, (b) CO, (c) NO₂, and (d) H₂ gases at various operating temperatures.

It is firmly established that reducing gases demonstrate a higher tendency to react with atomic oxygen ions (O[−]) compared to oxygen molecule ions (O₂[−]) on the oxide surface. This phenomenon is primarily responsible for the rise in sensor resistance in the presence of air, as it involves the trapping of electrons, leading to a reduction in the electron density within the n-type crystals. Consequently, when reducing gases interact with the oxide surface, they interact with O[−] ions, producing neutral compounds (such as H₂O and CO₂, contingent on gas type) [45–47]. This interaction subsequently injects electrons back into the crystals, resulting in a reduction in resistance attributed to the increased density of conduction electrons.

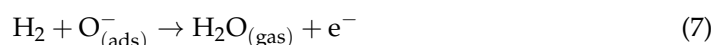
The gas sensing response of ZnO nanoparticles (NPs) to 1% CH₄ gas exposure was measured under typical operating temperatures ranging from 200 °C to 350 °C, as depicted in Figure 5a. With the increase in temperature within this range, both the sensing performance and the response and recovery times exhibited enhancement. The observed decline in sensor resistance during CH₄ exposure was also attributed to the methane molecule dissociation [47–49]. This dissociation leads to a reaction with adsorbed oxygen ions, releasing trapped electrons and consequently resulting in a reduction in resistance. The proposed reaction mechanism can be summarized as:



The gas sensing signal of ZnO NPs when exposed to 0.1% CO gas within the operating temperature range of 200–350 °C is given in Figure 5b. An increase in operating temperature results in an enhanced sensing response [50]. A mechanism for the interaction of reducing gases such as CO with oxygen species on an oxide surface can be succinctly summarized as follows [50]:



Following the interaction of CO gas with the ionic species, an electron is liberated into the oxide's conduction band, consequently enhancing its conductivity, as illustrated in Figure 5b. Remarkably, the ZnO nanoparticles (NPs) synthesized in this study exhibited no response to H₂ gas, as shown in Figure 5d. The fundamental reaction between H₂ gas and the surface of oxide can be elucidated as a single-step process, involving the interaction of hydrogen molecules with pre-adsorbed oxygen species [51], as demonstrated below:



In this reaction, the final product is gaseous H₂O, leading to the accumulation of electrons at the surface. This electron accumulation is responsible for the observed increase in conductivity, which was not observed well here.

Figure 5c exhibits the sensor signal towards NO₂ gas. Contrary to the behavior in reducing gas, the sensor resistance in oxidizing gas increased when exposed to the gas. The increase in resistance of oxide upon exposure to NO₂ can be ascribed to the formation of NO₂[−] or O[−]. It was reported that at a low temperature, the resistance of n-type oxide increases because of the following reaction [44,52]:



As this reaction is activated by thermal energy, the sensor response increases. When NO₂ is removed, the reverse of this reaction does not occur, and the following reaction leads to desorption of NO₂[−]. This increased Fermi energy and led to a decrease in resistance.

The terms “response time” and “recovery time” are commonly used in the context of gas sensors to describe the sensor's ability to detect and recover from exposure to a particular gas or concentration change. These parameters are crucial in understanding how quickly a gas sensor can react to changes in its environment. The response time of a gas sensor is the time it takes for the sensor to register a specified percentage (often 90%) of the total change in the resistance after exposure to a gas. The recovery time of a gas sensor is the time taken by the sensor to return to a specified percentage (again, often 90%) of its baseline reading after exposure to the gas is stopped. The response and recovery times are represented in Table 1 for the three gases of CH₄, CO, and NO₂. The response times obtained were between 300–150 s, 290–180 s, and 611–235 s corresponding to 200–350 °C for CH₄, CO, and NO₂, respectively. The recovery times recorded, 350–22 s, 279–11 s, and 142–16 s, correspond to 200–350 °C for CH₄, CO, and NO₂, respectively.

Table 1. The response (τ_{res}) and recovery time (τ_{rec}) constants toward CH₄, CO, and NO₂.

Temp	200 °C		250 °C		300 °C		350 °C	
	τ_{res} (s)	τ_{rec} (s)	τ_{res} (s)	τ_{rec} (s)	τ_{res} (s)	τ_{rec} (s)	τ_{res} (s)	τ_{rec} (s)
CH ₄	300	350	140	109	137	41	130	22
CO	290	279	160	58	158	33	160	11
NO ₂	>600	142	200	27	204	22	235	16

Understanding and characterizing the temperature dependence of nanoparticles in a sensor system is essential for optimizing the sensor's performance and ensuring accurate and reliable measurements. The curve involves characterizing the sensor's behavior at

different temperatures. If the sensor is detecting gases, the diffusion of gases through the nanoparticle layer is temperature-dependent. This can affect the rate at which the sensor responds to changes in the surrounding environment. Thus, the influence of operating temperature on sensor response is a crucial parameter for characterizing gas sensors and optimizing their performance. Figure 6 illustrates the reaction of the created sensor constructed across a range of operating temperatures, spanning 200 °C to 350 °C. The response was precisely computed for CH₄, H₂, CO, and NO₂ gases. It is noteworthy that for the NP sensor, the highest response towards CH₄ and CO gases is observed within the temperature range of 200 °C to 250 °C; however, the sensor showed lower responses towards NO₂ and H₂ gases.

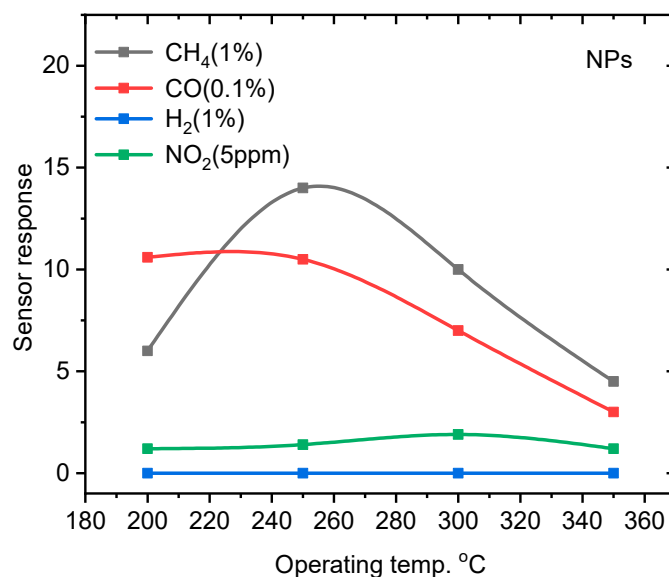


Figure 6. Dependence of sensor response on the operating temperature for various gases in the case of nanoparticle sensors.

Achieving high selectivity is crucial for ensuring the reliability and accuracy of gas measurements in various applications. Some gas sensors operate at elevated temperatures, and the choice of operating temperature can influence the selectivity. Temperature modulation can be used to enhance the response to specific gases while minimizing interference from others. Figure 7 illustrates the sensor response to different gases under varying operating temperatures, providing response values specific to NP sensors. The highest response for CH₄ was observed at 250 °C, while for CO gas it was observed at 200 °C. The sensor is less sensitive toward NO but exhibited a marginal increase in selectivity at 300 °C. Notably, the sensor exhibits a higher level of selectivity towards CO and CH₄ gases with temperature preferences.

Repeatability is an important performance characteristic of gas sensors and refers to the ability of a sensor to provide consistent and reproducible measurements when exposed to the same or similar conditions over a short period. In other words, a gas sensor is considered repeatable if it produces nearly identical responses to the same concentration of a target gas under consistent operating conditions. Enhancing the repeatability of gas sensors makes them more reliable and accurate in various applications such as environmental monitoring, industrial safety, and healthcare. Figure 8a shows that the sensor output is reliable, where it shows repeated signals upon exposure to the gas. For NO₂ gas, it may be that the sensor needs more time to recover, thus leading to a delay in full recovery as observed.

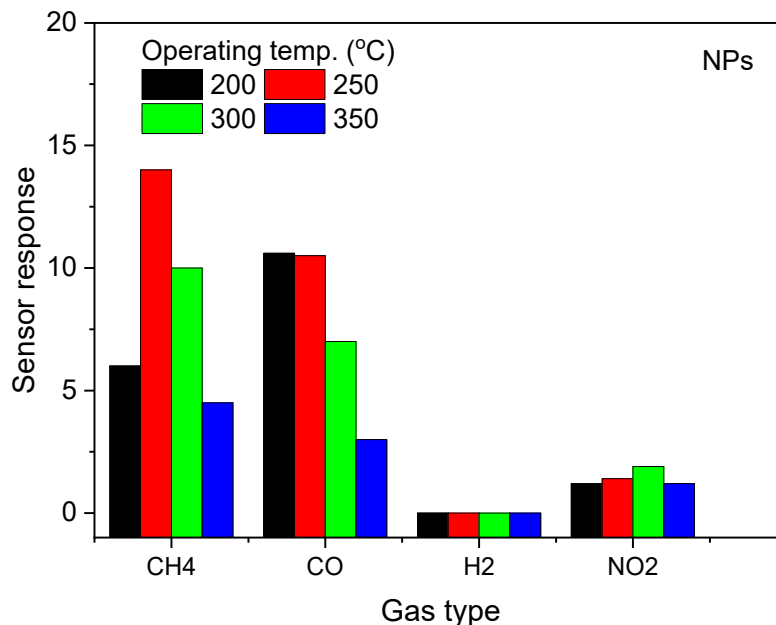


Figure 7. Sensor response variation in the NP sensors with exposure to 1.0% CH₄, 1.0% H₂, 1000 ppm CO, and 5 ppm NO₂ at various operating temperatures.

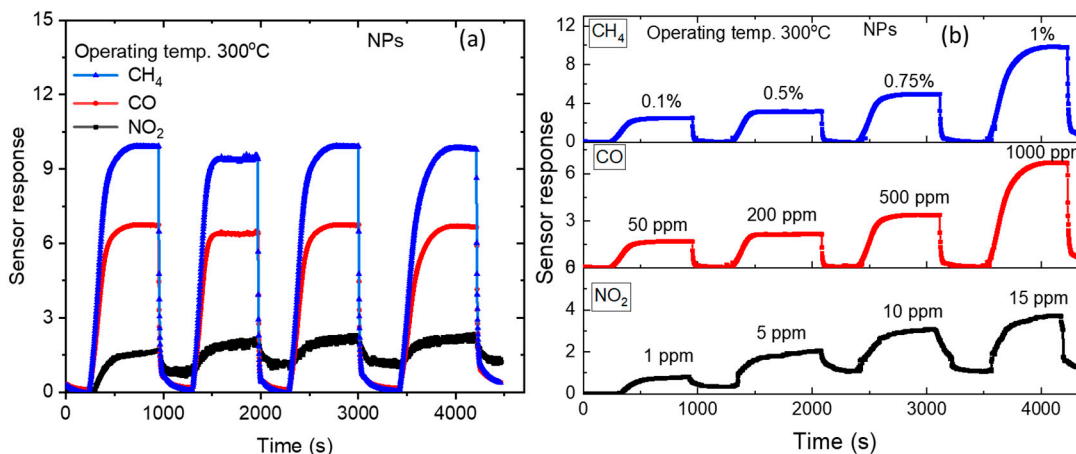


Figure 8. (a) The sensor repeatability towards CH₄ (1%), CO (0.1%), and NO₂ (5 ppm) and (b) the response signals of ZnO NPs at varying concentrations of CH₄, CO, and NO₂ at 300 °C.

Regular calibration against known gas concentrations is essential for maintaining and improving sensor selectivity. A calibration curve for a gas sensor is a graphical representation of the relationship between the sensor's response and the concentration of the target gas. The purpose of creating a calibration curve is to establish a correlation between the sensor's output and the actual concentration of the gas being measured. This curve is crucial for accurately converting sensor readings into meaningful gas concentration values. Figure 8b portrays the signal response of the ZnO sensor under various concentrations of CH₄, CO, and NO₂ gases at the particular operating temperature of 300 °C. Upon exposure to reducing gases, the response was found to increase upon increasing the concentration of the gases. The concentration inserted into the sensor was between 0.1% and 1% for CH₄ gas and 50 ppm and 1000 ppm for CO. The sensor exhibited an ability to detect high and low gas concentrations. The gas concentration of NO₂ ranged from 1 ppm to 15 ppm. From Figure 8b, one can observe that even the sensor has a good response to low concentrations and can still detect much lower concentrations of these gases. For NO₂, the sensor does not recover quickly to the baseline because it needs a longer time to recover. At high

temperatures and in the existence of NO₂, the surface of the sensor is sometimes poisoned, causing the recovery time to increase [44]. The calibration curves for the gases are provided in Figure 9. The sensor responses increased with increasing gas concentrations.

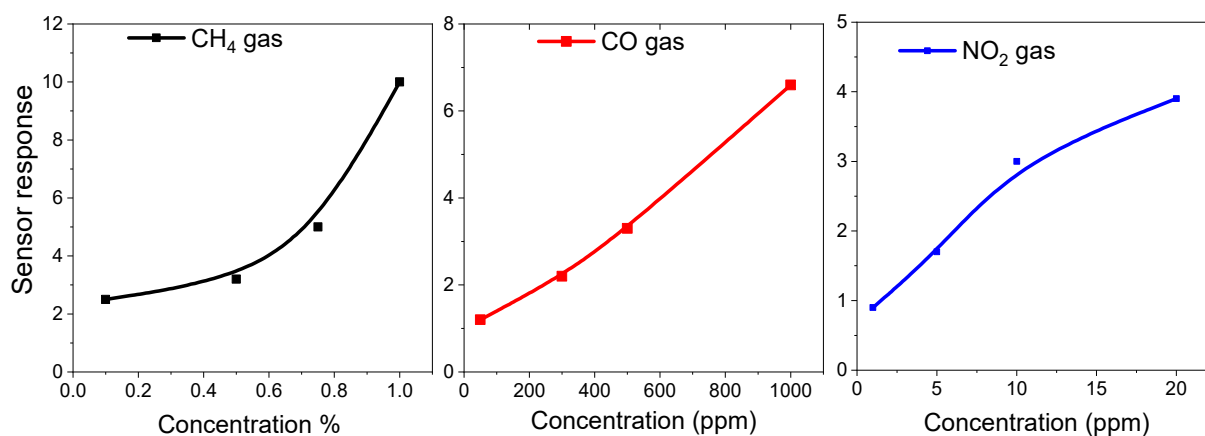


Figure 9. The calibration curve of NPs toward CH₄, CO, and NO₂ at 300 °C.

The sensitivity and selectivity of this fabricated nanostructure by the green method are proposed here. The sensor showed good sensitivity toward methane and carbon monoxide and lower sensitivity toward low NO₂ concentration (1–5 ppm), as shown in Figures 8 and 9. We can point out that even the sensor response toward 1 ppm NO₂ gas seems as low as ~1.0, which corresponds to 100% if we consider the percentage ($\Delta R/R \times 100$). This value is still high, which means the sensor is sensitive to lower concentrations. For example, at 1000 ppm (=0.1%) for CO and CH₄, the sensor response is 6.6 and 2.5, respectively. Also, at 50 ppm and 20 ppm of CO and NO₂, the sensor response is 1.2 and 3.9, respectively. This can explain the selectivity of ZnO toward CO compared to CH₄ and the selectivity toward NO₂ oxidizing gas compared to reducing gases.

Figure 10 shows the effect of humidity on the conductivity of the sensor and the response toward NO₂ gas, as an example. Humidity can impact the performance of ZnO gas sensors, influencing their sensitivity [53,54]. The interaction between water molecules and the ZnO surface could modify its electronic properties. Water molecules can adsorb onto the surface of ZnO through physical adsorption or chemisorption. Chemisorption may lead to the dissociation of water molecules into hydroxide (OH⁻) ions on the ZnO surface. This process is influenced by the presence of defects, such as oxygen vacancies, on the ZnO lattice [53,54]. Hydroxyl groups introduced on the surface may act as charge carriers, increasing the conductivity. The inset in Figure 10 demonstrates that the sensor resistance decreases when exposed to the water molecules. The sensor response toward the only humidity is about 0.04 (4%) at 60%Rh. However, water vapor molecules can compete with the target gas molecules for active sites on the sensor surface, reducing the sensor's ability to detect the target gases, as shown in Figure 10. In this figure, the sensor response toward NO₂ was affected by increasing the humidity, where the response slightly decreased from 2 to 1.45, which corresponds to 25% of the response in dry air.

Table 2 shows a comparison between the different structures of ZnO, including NO₂, CO, and CH₄. It also appears that the operating temperature of the sensor ranges from 200 to 450 °C. The sensitivity range of NO₂ concentrations is 1 to 200 ppm, and the sensor response ranges from 0.3 to 130. As for CO, the concentration of the gas ranges from 6 to 1000 ppm, and the sensor response ranges from 0.18 to 88. As for methane, the concentration ranges from 0.3 to 1%, and the sensitivity ranges from 0.6 to 7. The sensor response depends on the structure, operating temperature, and gas concentration, as shown in Table 2. The ZnO sensor in this current study is considered to have good performance compared to some previous sensors. The sensor also demonstrates that it has different operating temperatures for the maximum response for each gas.

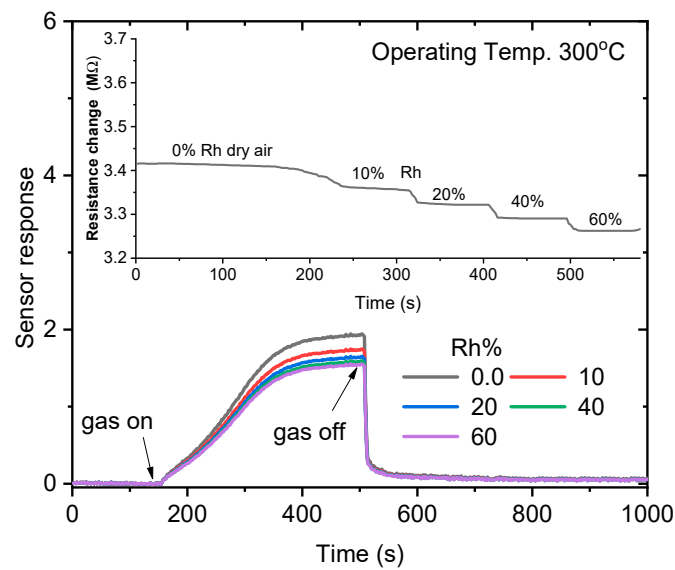


Figure 10. The effect of humidity on the sensor response toward 5 ppm of NO_2 at 300 °C. The inset is the effect of different levels of humidity on the sensor's resistance in the air.

Table 2. The performance of the ZnO sensor compared to previous published work.

ZnO Material	Operating Temp. (°C)	Gas (Concentration)	Response/Sensitivity $\Delta R/R$	Refs.
NO ₂ gas (ppm)				
Nanorods	200	1.0	0.3	[55]
	350	10	130.0	[56]
Nanowires	300	2	18.7	[57]
Nanobelt	350	10	0.81	[58]
Nanoneedle	200	200	0.64	[59]
Nanoparticles	200	100	0.37	[60]
Nanotetrapods	300	20	20.0	[61]
Thin film	450	200	90.0	[62]
Nanoparticles	300	5	1.9	Present work
		1	0.9	
		5	1.7	
		10	3	
		20	3.9	
CO gas (ppm)				
Thin film	450	200	88.0	[62]
Nanoparticles	350	250	7.0	[63]
Nanoflowers	300	200	8.0	[64]
Nanorods	300	100	49.0	[65]
Nanoparticles	110	100	0.3	[66]
Nanotubes	RT	6	0.18	[67]
Nanoparticles	250	80	2.8	[50]
Microspheres	150	100	14	[68]

Table 2. Cont.

ZnO Material	Operating Temp. (°C)	Gas (Concentration)	Response/Sensitivity $\Delta R/R$	Refs.
Nanoparticles	200	1000	10.6	Present work
		50	1.2	
	300	300	2.2	
		500	3.3	
		1000	6.6	
CH ₄ gas (%)				
Microstructure	314	0.5	1.8	[69]
Nanocrystals	250	1.0	0.87	[70]
Nanowalls	300	0.3	8.1	[71]
Thin film	350	1.0	0.6	[72]
Microspheres	200	0.5	7.0	[68]
		250	14	
	300	0.1	2.5	
		0.5	3.2	
		0.75	5	
		1	10	

4. Conclusions

In summary, we have successfully prepared ZnO nanoparticles (NPs) using a plant extract via a low-temperature green method. These NPs were subjected to thorough characterization using XRD, FESEM, TEM, and Raman spectroscopy techniques. XRD and Raman studies show that the green synthesized nanoparticles of ZnO are highly crystalline and have a single-phase nature without any impurities. The gas sensing performance of these sensors was systematically investigated in the presence of CH₄, H₂, CO, and NO₂ gases across various operating temperatures. The results of sensing studies revealed that the nanoparticles exhibit heightened sensitivity at temperatures of 200 °C, 250 °C, and 300 °C for CO, CH₄, and NO₂, respectively. This pointed out that the sensor achieved selectivity under varying operating temperatures, depending on the gas type. The repeatability studies of the fabricated sensor show excellent results for many cycles. The sensor showed a selectivity toward CO compared to CH₄ and a selectivity toward NO₂ oxidizing gas compared to all reducing gases. Enhancing the repeatability of gas sensors makes them more reliable and accurate in various applications such as environmental monitoring, industrial safety, and healthcare. A calibration curve was demonstrated upon exposure to reducing gases. The humidity affected the sensor conductivity, where the oxygen vacancies on the surface of ZnO can decompose water molecules to produce conductive ions, which enhances the conductivity of the sensor. The sensor response was also affected by the humidity due to the competition between water and gas molecules.

Author Contributions: Conceptualization, N.M.S., S.S., F.A. and A.A.; methodology, F.A., N.M.S. and S.S.; formal analysis, A.K.D.A., M.W.A.K., A.A. and K.M.A.; investigation, N.M.S., S.S., F.A. and M.W.A.K.; resources, A.K.D.A., M.W.A.K., K.M.A. and K.A.-M.; data curation, A.K.D.A., S.S. and K.A.-M.; writing—original draft preparation, N.M.S., F.A. and S.S.; writing—review and editing, A.K.D.A., A.A., K.A.-M., K.M.A. and M.W.A.K. All authors have read and agreed to the published version of the manuscript.

Funding: This research has been funded by the Scientific Research Deanship at the University of Ha'il—Saudi Arabia through project number MDR-22 016.

Institutional Review Board Statement: Not applicable.

Informed Consent Statement: Not applicable.

Data Availability Statement: Data will be available upon request.

Conflicts of Interest: All authors declare that there were no conflicts of interest.

References

1. Kumar, R.; Kumar, G.; Umar, A. Zinc Oxide Nanostructures for NO₂ Gas—Sensor Applications. *Nano-Micro Lett.* **2015**, *7*, 97–120. [[CrossRef](#)] [[PubMed](#)]
2. Brookes, C.; Wells, P.P.; Cibin, G.; Dimitratos, N.; Jones, W.; Morgan, D.J.; Bowker, M. Molybdenum Oxide on Fe₂O₃ Core—Shell Catalysts: Probing the Nature of the Structural Motifs Responsible for Methanol Oxidation Catalysis. *ACS Catal.* **2014**, *4*, 243–250. [[CrossRef](#)]
3. Roy, P.; Berger, S.; Schmuki, P. TiO₂ nanotubes: Synthesis and applications. *Angew. Chem. Int. Ed. Engl.* **2011**, *50*, 2904–2939. [[CrossRef](#)]
4. Spencer, M.J.S. Gas sensing applications of 1D-nanostructured zinc oxide: Insights from density functional theory calculations. *Prog. Mater. Sci.* **2012**, *57*, 437–486. [[CrossRef](#)]
5. Segets, D.; Gradl, J.; Taylor, R.K.; Vassilev, V.; Peukert, W. Analysis of Optical Absorbance Spectra for the Determination of ZnO Nanoparticle Size Distribution, Solubility, and Surface Energy. *ACS Nano* **2009**, *3*, 1703–1710. [[CrossRef](#)]
6. Wang, J.; Cao, J.; Fang, B.; Lu, P.; Deng, S.; Wang, H. Synthesis and characterization of multipod, flower-like, and shuttle-like ZnO frameworks in ionic liquids. *Mater. Lett.* **2005**, *59*, 1405–1408. [[CrossRef](#)]
7. Bacaksiz, E.; Parlak, M.; Tomakin, M.; Özçelik, A.; Karakız, M.; Altunbaş, M. The effects of zinc nitrate, zinc acetate and zinc chloride precursors on investigation of structural and optical properties of ZnO thin films. *J. Alloys Compd.* **2008**, *466*, 447–450. [[CrossRef](#)]
8. Lee, J.; Tak, Y. Electrodeposition of ZnO on ITO Electrode by Potential Modulation Method. *Electrochem. Solid-State Lett.* **2001**, *4*, C63. [[CrossRef](#)]
9. Chen, Y.W.; Liu, Y.C.; Lu, S.X.; Xu, C.S.; Shao, C.L.; Wang, C.; Zhang, J.Y.; Lu, Y.M.; Shen, D.Z.; Fan, X.W. Optical properties of ZnO and ZnO:In nanorods assembled by sol-gel method. *J. Chem. Phys.* **2005**, *123*, 134701. [[CrossRef](#)]
10. Lakshmi, B.B.; Dorhout, P.K.; Martin, C.R. Sol–Gel Template Synthesis of Semiconductor Nanostructures. *Chem. Mater.* **1997**, *9*, 857–862. [[CrossRef](#)]
11. Park, J.-A.; Moon, J.; Lee, S.-J.; Lim, S.-C.; Zyung, T. Fabrication and characterization of ZnO nanofibers by electrospinning. *Curr. Appl. Phys.* **2009**, *9*, S210–S212. [[CrossRef](#)]
12. Rajesh, D.; Vara Lakshmi, B.; Sunandana, C.S. Two-step synthesis and characterization of ZnO nanoparticles. *Phys. B Condens. Matter* **2012**, *407*, 4537–4539. [[CrossRef](#)]
13. Wu, J.-J.; Liu, S.-C. Low-Temperature Growth of Well-Aligned ZnO Nanorods by Chemical Vapor Deposition. *Adv. Mater.* **2002**, *14*, 215–218. [[CrossRef](#)]
14. Khorsand Zak, A.; Abd Majid, W.H.; Wang, H.Z.; Yousefi, R.; Moradi Golsheikh, A.; Ren, Z.F. Sonochemical synthesis of hierarchical ZnO nanostructures. *Ultrason. Sonochem.* **2013**, *20*, 395–400. [[CrossRef](#)]
15. Kooti, M.; Naghdi Sedeh, A. Microwave-Assisted Combustion Synthesis of ZnO Nanoparticles. *J. Chem.* **2013**, *2013*, 562028. [[CrossRef](#)]
16. Shetty, A.; Nanda, K.K. Synthesis of zinc oxide porous structures by anodization with water as an electrolyte. *Appl. Phys. A* **2012**, *109*, 151–157. [[CrossRef](#)]
17. Kumar, S.S.; Venkateswarlu, P.; Rao, V.R.; Rao, G.N. Synthesis, characterization and optical properties of zinc oxide nanoparticles. *Int. Nano Lett.* **2013**, *3*, 30. [[CrossRef](#)]
18. Gunalan, S.; Sivaraj, R.; Rajendran, V. Green synthesized ZnO nanoparticles against bacterial and fungal pathogens. *Prog. Nat. Sci. Mater. Int.* **2012**, *22*, 693–700. [[CrossRef](#)]
19. Ain Samat, N.; Md Nor, R. Sol–gel synthesis of zinc oxide nanoparticles using Citrus aurantifolia extracts. *Ceram. Int.* **2013**, *39*, S545–S548. [[CrossRef](#)]
20. Rajiv, P.; Rajeshwari, S.; Venkatesh, R. Bio-fabrication of zinc oxide nanoparticles using leaf extract of *Parthenium hysterophorus* L. and its size-dependent antifungal activity against plant fungal pathogens. *Spectrochim. Acta A Mol. Biomol. Spectrosc.* **2013**, *112*, 384–387. [[CrossRef](#)]
21. Pan, X.; Liu, X.; Bermak, A.; Fan, Z. Self-Gating Effect Induced Large Performance Improvement of ZnO Nanocomb Gas Sensors. *ACS Nano* **2013**, *7*, 9318–9324. [[CrossRef](#)]
22. Hosseini, Z.S.; Mortezaali, A.; Irajizad, A.; Fardindoost, S. Sensitive and selective room temperature H₂S gas sensor based on Au sensitized vertical ZnO nanorods with flower-like structures. *J. Alloys Compd.* **2015**, *628*, 222–229. [[CrossRef](#)]
23. Guo, W.; Liu, T.; Zhang, H.; Sun, R.; Chen, Y.; Zeng, W.; Wang, Z. Gas-sensing performance enhancement in ZnO nanostructures by hierarchical morphology. *Sens. Actuators B Chem.* **2012**, *166–167*, 492–499. [[CrossRef](#)]
24. Bai, S.; Guo, T.; Zhao, Y.; Sun, J.; Li, D.; Chen, A.; Liu, C.C. Sensing performance and mechanism of Fe-doped ZnO microflowers. *Sens. Actuators B Chem.* **2014**, *195*, 657–666. [[CrossRef](#)]

25. Guo, W.; Liu, T.; Wang, J.; Yu, W.; Sun, R.; Chen, Y.; Hussain, S.; Peng, X.; Wang, Z. Hierarchical ZnO porous microspheres and their gas-sensing properties. *Ceram. Int.* **2013**, *39*, 5919–5924. [[CrossRef](#)]
26. Roy, S.; Banerjee, N.; Sarkar, C.K.; Bhattacharyya, P. Development of an ethanol sensor based on CBD grown ZnO nanorods. *Solid-State Electron.* **2013**, *87*, 43–50. [[CrossRef](#)]
27. Tarwal, N.L.; Rajgure, A.V.; Patil, J.Y.; Khandekar, M.S.; Suryavanshi, S.S.; Patil, P.S.; Gang, M.G.; Kim, J.H.; Jang, J.H. A selective ethanol gas sensor based on spray-derived Ag–ZnO thin films. *J. Mater. Sci.* **2013**, *48*, 7274–7282. [[CrossRef](#)]
28. Chen, X.; Liu, J.; Jing, X.; Wang, J.; Song, D.; Liu, L. Self-assembly of ZnO nanosheets into flower-like architectures and their gas sensing properties. *Mater. Lett.* **2013**, *112*, 23–25. [[CrossRef](#)]
29. Luo, J.; Ma, S.Y.; Li, F.M.; Li, X.B.; Li, W.Q.; Cheng, L.; Mao, Y.Z.; Gz, D.J. The mesoscopic structure of flower-like ZnO nanorods for acetone detection. *Mater. Lett.* **2014**, *121*, 137–140. [[CrossRef](#)]
30. Kim, K.-M.; Kim, H.-R.; Choi, K.-I.; Kim, H.-J.; Lee, J.-H. ZnO hierarchical nanostructures grown at room temperature and their C₂H₅OH sensor applications. *Sensors Actuators B Chem.* **2011**, *155*, 745–751. [[CrossRef](#)]
31. Wei, S.; Wang, S.; Zhang, Y.; Zhou, M. Different morphologies of ZnO and their ethanol sensing property. *Sens. Actuators B Chem.* **2014**, *192*, 480–487. [[CrossRef](#)]
32. Miao, X.-J.; Zhao, X.-J.; Qin, H.; Jin, Q.; Chen, Y.; Cao, Z.-Q.; Yang, W.-T.; Wang, Q.-J.; Pan, Q.-H. Synergistic effect of cubic C₃N₄/ZnO/C hybrid composite for selective detection of sulfur dioxide. *Rare Met.* **2022**, *41*, 3662–3670. [[CrossRef](#)]
33. Del Zompo, F.; Ojetti, V.; Feliciani, D.; Mangiola, F.; Petruzzello, C.; Tesori, V.; Gaetani, E.; Gasbarrini, A.; Franceschi, F. Helicobacter pylori infection is associated with high methane production during lactulose breath test. *Eur. Rev. Med. Pharmacol. Sci.* **2016**, *20*, 3452–3456.
34. Coskun, A.; Demirci, B.; Turkdogan, K.A. Association of carbon monoxide poisonings and carboxyhemoglobin levels with COVID-19 and clinical severity. *World J. Methodol.* **2023**, *13*, 248–258. [[CrossRef](#)]
35. Chatterjee, S.; Park, S.; Low, K.; Kong, Y.; Pimentel, M. The degree of breath methane production in IBS correlates with the severity of constipation. *Am. J. Gastroenterol.* **2007**, *102*, 837–841. [[CrossRef](#)]
36. Attaluri, A.; Jackson, M.; Valestin, J.; Rao, S.S.C. Methanogenic flora is associated with altered colonic transit but not stool characteristics in constipation without IBS. *Am. J. Gastroenterol.* **2010**, *105*, 1407–1411. [[CrossRef](#)]
37. Mathur, R.; Amichai, M.; Chua, K.S.; Mirocha, J.; Barlow, G.M.; Pimentel, M. Methane and hydrogen positivity on breath test is associated with greater body mass index and body fat. *J. Clin. Endocrinol. Metab.* **2013**, *98*, E698–E702. [[CrossRef](#)]
38. Basseri, R.J.; Basseri, B.; Pimentel, M.; Chong, K.; Youdim, A.; Low, K.; Hwang, L.; Soffer, E.; Chang, C.; Mathur, R. Intestinal methane production in obese individuals is associated with a higher body mass index. *Gastroenterol. Hepatol.* **2012**, *8*, 22–28.
39. Patterson, A.L. The scherrer formula for X-ray particle size determination. *Phys. Rev.* **1939**, *56*, 978–982. [[CrossRef](#)]
40. Zhang, X.; Liu, Y.; Chen, S. A novel method for measuring distribution of orientation of one-dimensional ZnO using resonance Raman spectroscopy. *J. Raman Spectrosc.* **2005**, *36*, 1101–1105. [[CrossRef](#)]
41. Zhang, R.; Yin, P.-G.; Wang, N.; Guo, L. Photoluminescence and Raman scattering of ZnO nanorods. *Solid State Sci.* **2009**, *11*, 865–869. [[CrossRef](#)]
42. Damen, T.C.; Porto, S.P.S.; Tell, B. Raman Effect in Zinc Oxide. *Phys. Rev.* **1966**, *142*, 570–574. [[CrossRef](#)]
43. Calleja, J.M.; Cardona, M. Resonant Raman scattering in ZnO. *Phys. Rev. B* **1977**, *16*, 3753–3761. [[CrossRef](#)]
44. Ruhland, B.; Becker, T.; Müller, G. Gas-kinetic interactions of nitrous oxides with SnO₂ surfaces. *Sens. Actuators B Chem.* **1998**, *50*, 85–94. [[CrossRef](#)]
45. Shaalan, N.M.; Yamazaki, T.; Kikuta, T. Influence of morphology and structure geometry on NO₂ gas-sensing characteristics of SnO₂ nanostructures synthesized via a thermal evaporation method. *Sensors Actuators B Chem.* **2011**, *153*, 11–16. [[CrossRef](#)]
46. Koziej, D.; Thomas, K.; Barsan, N.; Thibault-Starzyk, F.; Weimar, U. Influence of annealing temperature on the CO sensing mechanism for tin dioxide based sensors—Operando studies. *Catal. Today* **2007**, *126*, 211–218. [[CrossRef](#)]
47. Haridas, D.; Gupta, V. Enhanced response characteristics of SnO₂ thin film based sensors loaded with Pd clusters for methane detection. *Sens. Actuators B Chem.* **2012**, *166–167*, 156–164. [[CrossRef](#)]
48. Shaalan, N.M.; Hamad, D.; Aljaafari, A.; Abdel-Latief, A.Y.; Abdel-Rahim, M.A. Preparation and Characterization of Developed Cu_xSn_{1-x}O₂ Nanocomposite and Its Promising Methane Gas Sensing Properties. *Sensors* **2019**, *19*, 2257. [[CrossRef](#)]
49. Shaalan, N.M.; Morsy, A.E.A.; Abdel-Rahim, M.A.; Rashad, M. Simple preparation of Ni/CuO nanocomposites with superior sensing activity toward the detection of methane gas. *Appl. Phys. A* **2021**, *127*, 455. [[CrossRef](#)]
50. Hjiri, M.; Bahanan, F.; Aida, M.S.; El Mir, L.; Neri, G. High Performance CO Gas Sensor Based on ZnO Nanoparticles. *J. Inorg. Organomet. Polym. Mater.* **2020**, *30*, 4063–4071. [[CrossRef](#)]
51. Aljaafari, A.; Ahmed, F.; Awada, C.; Shaalan, N.M. Flower-Like ZnO Nanorods Synthesized by Microwave-Assisted One-Pot Method for Detecting Reducing Gases: Structural Properties and Sensing Reversibility. *Front. Chem.* **2020**, *8*, 456. [[CrossRef](#)]
52. Shaalan, N.M.; Yamazaki, T.; Kikuta, T. Effect of micro-electrode geometry on NO₂ gas-sensing characteristics of one-dimensional tin dioxide nanostructure microsensors. *Sens. Actuators B Chem.* **2011**, *156*, 784–790. [[CrossRef](#)]
53. Zhang, Y.; Li, Z. Effects of pH on High-Performance ZnO Resistive Humidity Sensors Using One-Step Synthesis. *Sensors* **2019**, *19*, 5267. [[CrossRef](#)]
54. Sonker, R.K.; Yadav, B.C.; Sharma, A.; Tomar, M.; Gupta, V. Experimental investigations on NO₂ sensing of pure ZnO and PANI–ZnO composite thin films. *RSC Adv.* **2016**, *6*, 56149–56158. [[CrossRef](#)]

55. Öztürk, S.; Kılınç, N.; Öztürk, Z.Z. Fabrication of ZnO nanorods for NO₂ sensor applications: Effect of dimensions and electrode position. *J. Alloys Compd.* **2013**, *581*, 196–201. [[CrossRef](#)]
56. Shi, L.; Naik, A.J.T.; Goodall, J.B.M.; Tighe, C.; Gruar, R.; Binions, R.; Parkin, I.; Darr, J. Highly Sensitive ZnO Nanorod- and Nanoprism-Based NO₂ Gas Sensors: Size and Shape Control Using a Continuous Hydrothermal Pilot Plant. *Langmuir* **2013**, *29*, 10603–10609. [[CrossRef](#)]
57. An, S.; Park, S.; Ko, H.; Jin, C.; Lee, W.I.; Lee, C. Enhanced gas sensing properties of branched ZnO nanowires. *Thin Solid Films* **2013**, *547*, 241–245. [[CrossRef](#)]
58. Sadek, A.Z.; Wlodarski, W.; Kalantar-zadeh, K.; Choopun, S. ZnO Nanobelt Based Conductometric H₂ and NO₂ Gas Sensors. In Proceedings of the Sensors, Irvine, CA, USA, 30 October—3 November 2005; pp. 1326–1329.
59. Pawar, R.C.; Lee, J.-W.; Patil, V.B.; Lee, C.S. Synthesis of multi-dimensional ZnO nanostructures in aqueous medium for the application of gas sensor. *Sens. Actuators B Chem.* **2013**, *187*, 323–330. [[CrossRef](#)]
60. Chougule, M.A.; Sen, S.; Patil, V.B. Fabrication of nanostructured ZnO thin film sensor for NO₂ monitoring. *Ceram. Int.* **2012**, *38*, 2685–2692. [[CrossRef](#)]
61. Calestani, D.; Zha, M.; Mosca, R.; Zappettini, A.; Carotta, M.C.; Di Natale, V.; Zanotti, L. Growth of ZnO tetrapods for nanostructure-based gas sensors. *Sens. Actuators B Chem.* **2010**, *144*, 472–478. [[CrossRef](#)]
62. Fomekong, R.L.; Saruhan, B. Influence of humidity on NO₂-sensing and selectivity of spray-CVD grown ZnO thin film above 400 °C. *Chemosensors* **2019**, *7*, 42. [[CrossRef](#)]
63. Ryu, H.W.; Park, B.S.; Akbar, S.A.; Lee, W.S.; Hong, K.J.; Seo, Y.J.; Shin, D.C.; Park, J.S.; Chio, G.P. ZnO sol-gel derived porous film for CO gas sensing. *Sens. Actuators B Chem.* **2003**, *96*, 717–722. [[CrossRef](#)]
64. Krishnakumar, T.; Jayaprakash, R.; Pinna, N.; Donato, N.; Bonavita, A.; Micali, G.; Neri, G. CO gas sensing of ZnO nanostructures synthesized by an assisted microwave wet chemical route. *Sens. Actuators B Chem.* **2009**, *143*, 198–204. [[CrossRef](#)]
65. Lim, S.K.; Hwang, S.H.; Kim, S.; Park, H. Preparation of ZnO nanorods by microemulsion synthesis and their application as a CO gas sensor. *Sens. Actuators B Chem.* **2011**, *160*, 94–98. [[CrossRef](#)]
66. Karaduman, I.; Yıldırım, M.A.; Yıldırım, S.T.; Ateş, A.; Özdemir, Y.A.; Acar, S. The effect of different doping elements on the CO gas sensing properties of ZnO nanostructures. *J. Mater. Sci. Mater. Electron.* **2017**, *28*, 18154–18163. [[CrossRef](#)]
67. Vijayakumar; Shivaraj, B.W.; Manjunatha, C.; Abhishek, B.; Nagaraju, G.; Panda, P.K. Hydrothermal synthesis of ZnO nanotubes for CO gas sensing. *Sens. Int.* **2020**, *1*, 100018. [[CrossRef](#)]
68. Wang, Y.; Cui, Y.; Meng, X.; Zhang, Z.; Cao, J. A gas sensor based on Ag-modified ZnO flower-like microspheres: Temperature-modulated dual selectivity to CO and CH₄. *Surf. Interfaces* **2021**, *24*, 101110. [[CrossRef](#)]
69. Gruber, D.; Kraus, F.; Müller, J. A novel gas sensor design based on CH₄/H₂/H₂O plasma etched ZnO thin films. *Sens. Actuators B Chem.* **2003**, *92*, 81–89. [[CrossRef](#)]
70. Bhattacharyya, P.; Basu, P.K.; Mondal, B.; Saha, H. A low power MEMS gas sensor based on nanocrystalline ZnO thin films for sensing methane. *Microelectron. Reliab.* **2008**, *48*, 1772–1779. [[CrossRef](#)]
71. Chen, T.P.; Chang, S.P.; Hung, F.Y.; Chang, S.J.; Hu, Z.S.; Chen, K.J. Simple fabrication process for 2D ZnO nanowalls and their potential application as a methane sensor. *Sensors* **2013**, *13*, 3941–3950. [[CrossRef](#)]
72. Teimoori, F.; Khojier, K.; Dehnavi, N.Z. Investigation on the Electrical and Methane Gas-Sensing Properties of ZnO Thin Films Produced by Different Methods. *J. Electron. Mater.* **2016**, *45*, 4881–4889. [[CrossRef](#)]

Disclaimer/Publisher’s Note: The statements, opinions and data contained in all publications are solely those of the individual author(s) and contributor(s) and not of MDPI and/or the editor(s). MDPI and/or the editor(s) disclaim responsibility for any injury to people or property resulting from any ideas, methods, instructions or products referred to in the content.